Grain refinement in laser powder bed fusion: The influence of dynamic recrystallization and recovery

Hossein Eskandari Sabzi [a], Nesma T. Aboulkhair [b], Xingzhong Liang [a,c], Xiao-Hui Li [d], Marco Simonelli [b], Hanwei Fu [d,*], Pedro E.J. Rivera-Díaz-del-Castillo [a,*]

[a] Department of Engineering, Engineering Building, Lancaster University, LA1 4YW, United Kingdom
[b] Centre for Additive Manufacturing (CfAM), Faculty of Engineering, University of Nottingham, NG8 1BB, United Kingdom
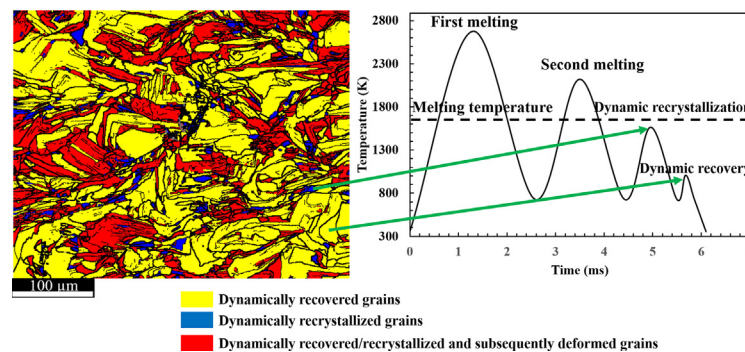[c] Department of Engineering, University of Leicester, Leicester LE1 7RH, UK
[d] School of Materials Science and Engineering, Beihang University, No. 37 Xueyuan Road, Beijing 100191, China

HIGHLIGHTS

- Detailed characterisation of recrystallized laser powder bed fusion 316L structure
- Dynamic recrystallization is essential to promote grain refinement in 316L.
- A methodology for tailoring grain refinement via recrystallization is suggested.
- Zener-Hollomon and thermostatistical approaches described grain refinement features.

GRAPHICAL ABSTRACT

■ Dynamically recovered grains
■ Dynamically recrystallized grains
■ Dynamically recovered/recrystallized and subsequently deformed grains

ARTICLE INFO

ABSTRACT

During laser powder bed fusion (LPBF) the powder bed undergoes several thermal cycles incorporating complex thermo-mechanical processing. Different restoration mechanisms such as dynamic recovery, dynamic recrystallization and grain growth can be activated at different thermal cycles, leading to a very fine average grain size. This is modelled via classical and thermostatistical approaches for an austenitic stainless steel. Four subsequent thermal cycles in each layer induce various microstructural transitions for each individual grain. The high cooling rate solidification in the first two thermal cycles leads to the formation of a highly deformed cellular microstructure. Discontinuous and continuous dynamic recrystallization are activated in the third thermal cycle to induce grain refinement. The fourth thermal cycle undergoes dynamic recovery and grain growth. The as-built alloys exhibit an excellent combination of high yield and ultimate tensile strength. The high strength is attributed to the activation of the various dynamic recrystallization mechanisms, as well as to the development of the cellular structures resulting from a high cooling rate upon solidification. A methodology to design alloys with tailored microstructures is presented.

1. Introduction

Laser powder bed fusion (LPBF) is a promising process likely to revolutionise manufacturing by producing geometrically complex-shaped parts with tailored mechanical properties through local microstructure control [1]. In this process, powder particles are melted to

* Corresponding authors.
E-mail addresses: fhwcambridge@hotmail.com (H. Fu), p.rivera1@lancaster.ac.uk (P.E.J. Rivera-Díaz-del-Castillo).

build three-dimensional components by repetitive scanning using a high-energy laser beam [2]. During LPBF, dislocation multiplication and thermally activated softening or restoration processes (dynamic recovery (DRV) and dynamic recrystallization (DRX)) take place due to the heating and cooling cycles [3]. These phenomena can be modelled and described using the well-known Kocks-Mecking equation [4,5].

In thermo-mechanical processes such as hot rolling or forging, a plastic strain is imposed on the material at high temperatures, and DRX may occur when a critical strain is reached [6]. Analytical expressions for the calculation of this critical strain as a function of strain rate and temperature include the classical Zener-Hollomon analysis [7] and the thermostatistical approach proposed by Galindo-Nava and Rivera-Díaz-del-Castillo [8,9]. Softening due to DRX results in variations in flow stress, which can directly influence the yield strength at room temperature through the final dislocation density [5].

The occurrence of DRX in LPBF has not been reported before. The contraction due to heat dissipation upon cooling leads to a severe plastic deformation, which combined with the high temperatures present in LPBF, can be considered as a thermo-mechanical process at ultra-high strain rates. In this paper, the conditions for the activation of DRX and DRV during LPBF are examined using both classical and thermostatistical theories. Thermal analysis is carried out using empirical and simulation results to describe the thermal cycles during layering in LPBF of 316L stainless steel (SS). Experiments with the optimised process parameters are carried out to investigate the possibility of activating DRX and DRV during LPBF, and their impact on the microstructure and tensile properties of the as-built samples. A composition-independent methodology is proposed to control microstructural evolution during LPBF and enhance mechanical properties.

2. Conditions for the activation of dynamic recrystallization and recovery

The conditions for the activation of restoration processes such as DRX and DRV have been investigated comprehensively for the thermo-mechanical processing of wrought metals and alloys [10–13]. In this work, two approaches are used for predicting the activation of restoration mechanisms: classical and thermostatistical.

2.1. Classical approach

Zener and Hollomon showed that hot deformation of steels can be interpreted via the strain rate $\dot{\varepsilon}$ and deformation temperature T, using a parameter, known as Zener-Hollomon parameter [7]:

$$Z = \dot{\varepsilon} \, \exp\left\{\frac{Q}{RT}\right\}, \tag{1}$$

where $Q=460$ kJ/mol [14] (for 316L deformed around 1522 K) is the activation energy for triggering deformation and $R = 8.314$ J/mol·K is the universal gas constant. Wang et al. [15] showed that LPBF in 316L SS leads to the segregation of Cr and Mo into solidification cell boundaries, which can lead to a high level of austenite stability. They also showed that the elemental segregation is closely dependent on process parameters such as the laser power and the scan speed. A decrease in laser power and scan speed can result in suppression of elemental segregation in 316L SS [15,16]. Sun et al. [17,18] also claimed that ultra-fast cooling rates of LPBF ($\geq 10^5$ K/s) suppress elemental segregation significantly. Thus, the value of 460 kJ/mol for Q for the conditions, where a low laser power and scan speed lead to cooling rates higher than 10^5 K/s is thought to be valid. Under conditions of low and medium Z values, DRX is likely to occur; otherwise, DRV is likely to be the main restoration mechanism. Several reports showed that when a critical strain is reached, discontinuous dynamic recrystallization (DDRX) can be activated leading to a very fine grain

microstructure [11,19–22]. Liu et al. [6] obtained the relationship between the critical strain ε_c for DDRX and the Zener-Hollomon parameter during hot compression testing at temperatures between 900 °C and 1200 °C of a 316L type of steel:

$$\varepsilon_c = 0.009Z^{0.084}. \tag{2}$$

If DDRX occurs under moderate Z values, the average grain size of 316LSS after the activation of DDRX (D_{DRX} [μm]) can be estimated via [14]:

$$D_{DRX} = 5.2 \times 10^3 (Z)^{-0.17}. \tag{3}$$

2.2. Thermostatistical approach

The thermostatistical approach for modelling hot deformation of face-centred cubic (FCC) materials has been developed by Galindo-Nava and Rivera-Díaz-del-Castillo [9]; it considers not only process parameters such as strain rate and temperature, but also the material's physical properties. This incorporates the degrees of freedom of a dislocation upon deformation. From such, ε_c for DDRX activation can be estimated via [8]:

$$\varepsilon_c = \frac{\frac{1}{2}\mu b^3 - \left(1 + \frac{1}{k_c}\right)T\Delta S}{\frac{1}{2}\mu b^3}, \tag{4}$$

where μ is the shear modulus, b is the magnitude of the Burgers vector, ΔS is the statistical entropy of dislocations and $k_c = \frac{12\pi(1-\nu)}{(2+\nu)}\left(1 + \frac{T\Delta S}{\mu b^3}\right)$ [8], where ν is the Poisson ratio. The dislocation statistical entropy can be calculated via:

$$\Delta S = k_B \ln\left(\frac{\dot{\varepsilon}_0 + \vartheta}{\dot{\varepsilon}}\right), \tag{5}$$

where $k_B = 1.38 \times 10^{-23}$ J/K is the Boltzmann constant, $\dot{\varepsilon}_0 = cb\rho_Y$ is the strain rate related to the speed of sound (c, see Table 2), and ρ_Y is the dislocation density at the yield point ($\rho_Y = (0.9\sigma_Y/\mu b)^2$), where σ_Y is the material's yield strength [8]; $\vartheta = 10^{13} \exp\left(-\frac{E_m}{RT}\right)$ is the frequency of atomic jump of vacancies and E_m is the vacancy migration energy.

An advantage of the thermostatistical theory of hot deformation is that it can also predict the conditions for the activation of continuous dynamic recrystallization (CDRX) and DRV [9]. The critical condition for the occurrence of CDRX is satisfied when the process strain rate is lower than the critical strain rate $\dot{\varepsilon}_c$:

$$\dot{\varepsilon}_c = (\dot{\varepsilon}_0 + \vartheta) \exp\left(-\frac{\frac{\lambda}{2}\mu b^3 - \frac{2xl^*}{bk_c}\Delta G_{sys}}{k_B T}\right), \tag{6}$$

where $\lambda = 0.6$ [9] is a length scaling constant, x is the solute concentration in molar fraction ($0 \leq x < 0.5$), $l^* = 12.5b$ is the dislocation's distortion length, which accounts for 98% of the total strain field induced by dislocations and ΔG_{sys} is the Gibbs free energy of the alloy, representing the energy barrier accounting for the possible atomic arrangements in the lattice. If the process strain rate is higher than the critical value, then DRV becomes the most favourable restoration process [9].

Table 1
Chemical composition of the powder in wt.%.

Fe	Cr	Ni	Mo	Mn	Si	P	S	N	C	Cu
Bal.	17.75	12.75	2.38	2	0.75	0.025	0.01	0.1	0.03	0.5

3. Experimental procedure

Gas atomised spherical 316L SS powder (10–45 μm) was provided by Carpenter Additive (Table 1). A Renishaw plc (UK) AM125 LPBF machine of 35 μm spot size was used for building; a 20 μm powder layer thickness was laid by a recoating blade on a 304L stainless steel substrate preheated to 80 °C. A 100 W laser power with 1 m/s beam speed was used under argon atmosphere. A laser scan strategy of meander, with rotation of 67° at each layer with a hatch distance of 70 μm, was applied. These process parameters were adopted following an optimisation procedure described in [23] to obtain a near-fully dense build. Producing a defect-free specimen is important for elimination of the complex influence of defects such as balling on microstructural evolution, as balling defects are known to induce surface tension, which results in variations in thermal gradients and the resulting microstructures [24,25]. Moreover, using these process parameters, the critical conditions for the activation of DRX mechanisms and DRV are met as will be discussed later. Flat tensile test specimens with a gauge length of 35 mm and thickness of 1.2 mm were fabricated by LPBF and tested at 10^{-4} s^{-1} at ambient temperature using an Instron 3382 universal testing machine, with load axis parallel to the build direction. The reported strength and ductility were the average of 3 tests. The Vickers hardness was measured with a load of 300 g. The values obtained for the hardness of the as-built samples are used to estimate the residual plastic strain accumulated during LPBF.

Optical microscopy was performed on the longitudinal section of the as-built samples for porosity characterisation after polishing. Electron backscattered diffraction (EBSD) was conducted on a cubic sample from the grip of the tensile specimen; its surface was ground with SiC paper followed by electro-polishing to remove grinding residual stresses. EBSD analysis was carried out in a Tescan Mira 3 LMHP field emission scanning electron microscope equipped with OXFORD Instruments symmetry EBSD detector at a scanning step size of 0.8 μm. The data were analysed using post-processing software Channel 5.

4. Results

4.1. Mechanical behaviour

A representative optical microscopy image of the polished surface is shown in Fig. 1a, where a few spherical pores can be seen (metallurgical pores). A near full density of 99.97% $\pm$ 0.02 allowed the mechanical properties of the as-built sample to be correlated with microstructural evolution. Fig. 1b and 1c show tensile engineering and true stress-strain responses in the as-built condition, respectively. The sample exhibited excellent mechanical properties. A yield strength of 600 $\pm$ 3 MPa and an ultimate tensile strength of 707 $\pm$ 3 MPa have been obtained, as well as high total elongation of 40 $\pm$ 2%. Fig. 1c also indicates two stages in strain hardening during plastic deformation. This combination of high yield and ultimate tensile strengths surpasses all the previously reported as-built LPBF processed 316L SS (Fig. 1d) [1,15,26–38].

4.2. Microstructural evolution

To understand the nature of such outstanding mechanical properties, EBSD was performed to reveal the microstructural evolution before tensile testing. A representative inverse pole figure (IPF) of the as-built sample and its corresponding grain size distribution is shown in Fig. 2. IPF shown in Fig. 2a indicates that the as-built microstructure has a mixture of columnar and equiaxed grains with a bimodal grain size distribution of nearly random misorientation. Fig. 2b reveals the grain size distribution, ranging from 1.5–92 μm, and an average grain size (d_{avg}) of 4.79 $\pm$ 2 μm, with a high fraction of fine grains (smaller than 8 μm).
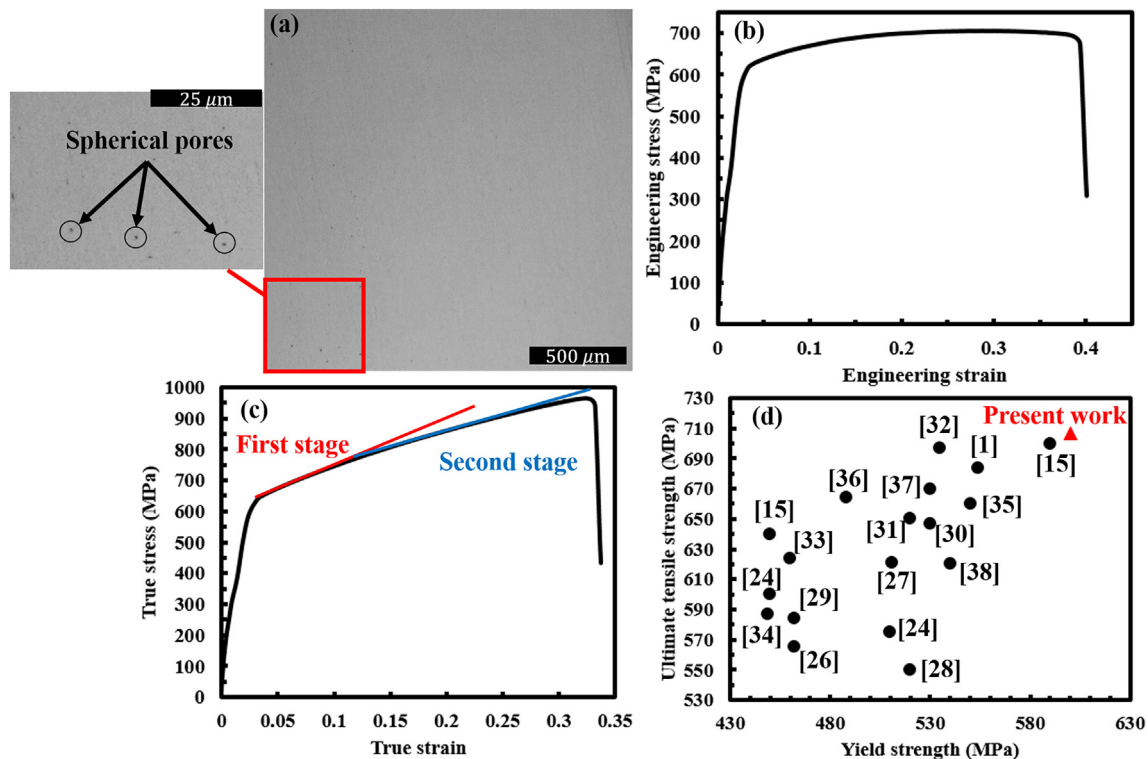

Fig. 1. (a) Optical micrograph showing near fully-dense sample produced by LPBF, (b) tensile engineering and (c) true stress-strain curves of the as-built sample. (d) Yield versus ultimate tensile strength for LPBF as-built samples reported in literature compared with this study.
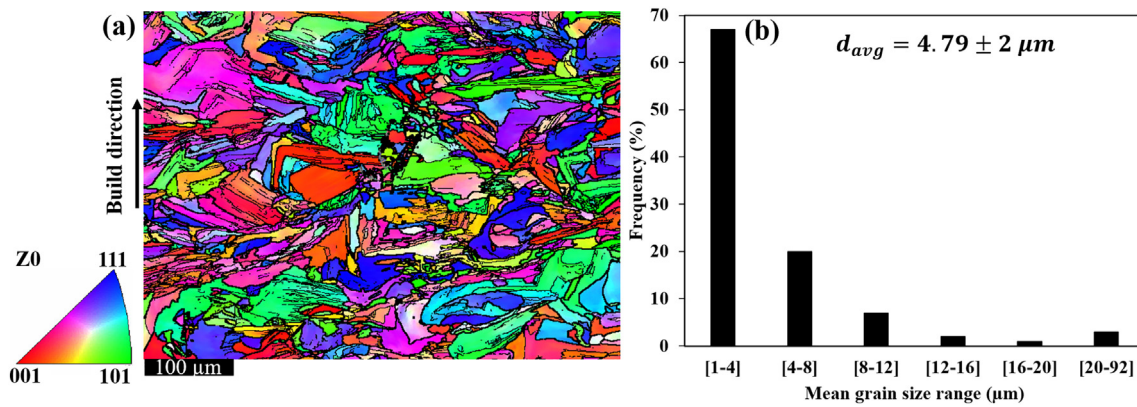
Fig. 2. (a) EBSD inverse pole figure (IPF) map of the as-built LPBF 316L SS sample, showing grain orientations. (b) Distribution of the mean grain size, showing 87% of the grains have a size smaller than 8 μm.

This is in contrast with similar reports indicating average grain sizes larger than 13 μm [15,28,31].

In order to reveal the reason for such grain refinement, a recrystallized fraction map was generated by EBSD (Fig. 3). Fully recrystallized grains are shown in blue, deformed regions in red and substructured (dynamically recovered with subgrains) grains in yellow. Channel 5 software measures the internal average misorientation angle within each grain; if it exceeds 15°, the grain is classified as deformed. For a grain with internal misorientation under 15° but misorientation across subgrains above 15°, the grain is categorised as substructured. All the remaining grains are classed as recrystallized. From Fig. 3, 59% of the grains are substructured, 5% recrystallized and 36% are deformed. Thus, the microstructure of the LPBF as-built 316L SS has a trimodal grain-type feature.

As recrystallized and recovered (substructured) grains are apparent in the LPBFed sample, a further investigation has been carried out to determine the occurrence of DRX and DRV, their sequence and nature. Fig. 4a shows the recrystallization map combined with the grain boundary map. The sample contains a large fraction of low angle grain boundaries (LAGBs) (green) with misorientations between 2 and 15°, which compose about 70% of the total grain boundaries (Fig. 4b). Most of the very small recrystallized grains contained LAGBs, while the rest have

high angle grain boundaries (HAGBs). This indicates that more than one DRX mechanism was activated during LPBF of 316L SS. The heavily dislocated deformed grains also have the same characteristics of recrystallized grains, whereas most of the substructured grains have HAGBs. Fig. 4c represents the twin boundary map of the as-built sample. A very low fraction of the total boundaries are characterised as annealing twins (about 1.71%).

As texture evolution is believed to influence DRX and DRV [10], the microtexture of the grains is shown in Fig. 5. The most dominant texture is ⟨110⟩-fibre (green), with a volume fraction of 32%. ⟨111⟩-fibre (blue), ⟨100⟩-fibre (red) and the Cube (pink) follow with 23, 18 and 10% fractions, respectively. It can be seen that there is no specific texture associated to any specific grain type, which suggests the activation of different DRX mechanisms during LPBF of 316L SS.

5. Modelling

5.1. Thermal profile, strain rate and thermal strain

During LPBF large thermal and residual plastic strains (ε_t and ε_p, respectively) can be generated as a result of succeeding thermal cycles that a layer experiences during processing [39]. Each layer experiences
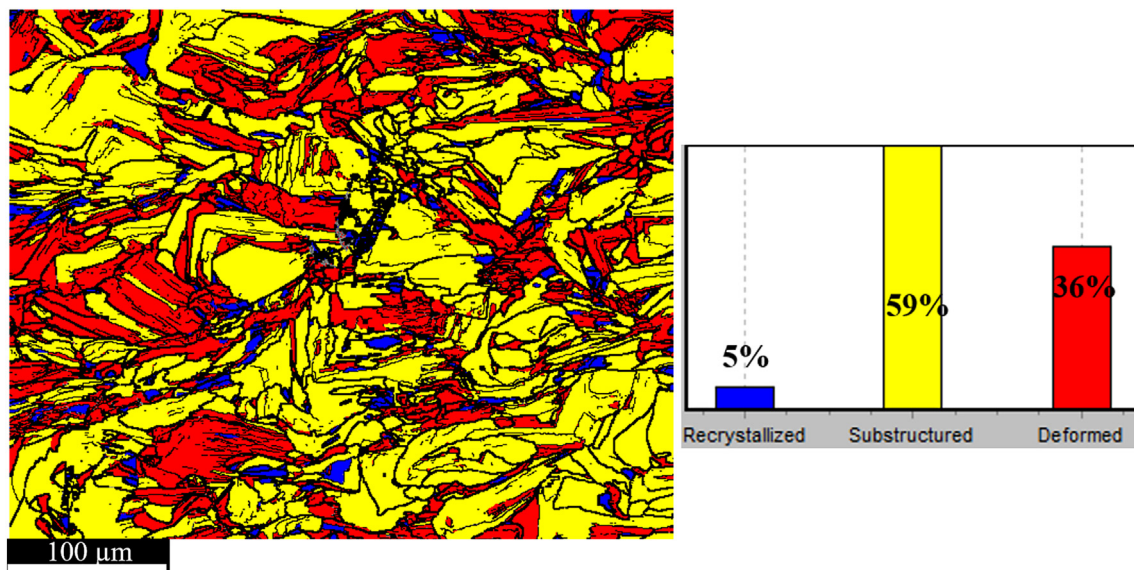

Fig. 3. Recrystallized fraction component map, showing the process-induced deformed, substructured and recrystallized grains. Bars indicate the corresponding volume fraction.
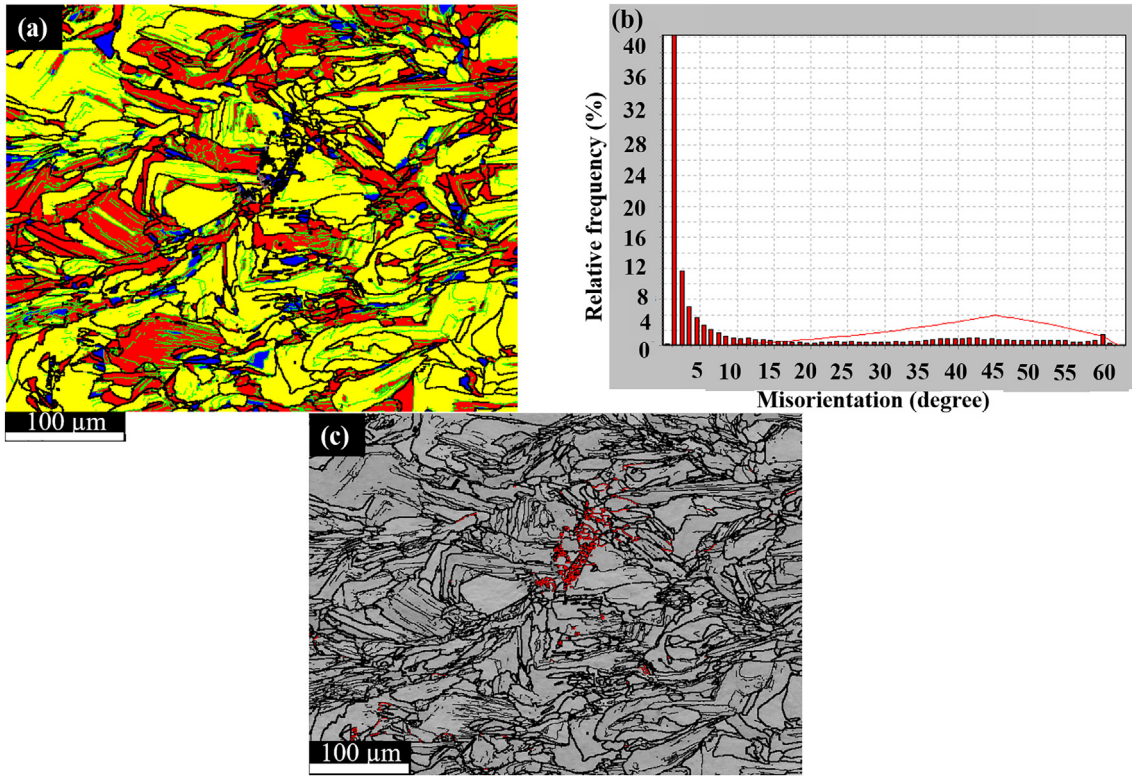
Fig. 4. (a) Recrystallized fraction component map combined with grain boundary map, indicating high angle grain boundaries (misoreintations >15°) in black and low angle grain boundaries (misorientations between 2 and 15°) in green. (b) Relative frequency of low and high angle grain boundaries (~70% and ~30%, respectively). (c) Twin boundary map, showing Σ3 boundaries. The red colour shows twin boundaries.

a peak temperature (T_{peak}), which then drops during subsequent thermal cycles upon layering; the corresponding temperatures depend on the process parameters and the physical properties of the alloy. The peak temperature, T_{peak}, is related to the process heat input via the relationship [40]:

$$T_{peak} = \frac{H_n T_b}{H_n^{max}}, \tag{7}$$

where H_n is the normalised enthalpy, which quantifies the process heat input, H_n^{max} is the maximum allowable heat input to prevent keyhole formation (evaporation) and T_b is the boiling temperature. H_n is defined as [41]:

$$H_n = \frac{AP}{h_s \sqrt{\pi \alpha v D^3}}, \tag{8}$$

where A is the absorptivity, P is the laser power, h_s is the enthalpy at the melting temperature, α is the thermal diffusivity, v is the scan speed and D is the laser spot size. The value of H_n^{max} is achieved for values of H_n consistent with the boiling temperature, T_b. H_n^{max} for a given composition is defined as [42]:

$$H_n^{max} = \frac{\pi T_b}{T_m}, \tag{9}$$

where T_m is the melting temperature. Referring to eq. (7), the peak temperature is assumed to vary within the range $T_m < T_{peak} < T_b$, where the lower limit corresponds to $H_n^{min} = \pi$ [41]. T_{peak} is therefore assumed to linearly vary with H_n with the proportionality constant being T_b/H_n^{max} [40].

Using the physical properties presented in Table 2, $H_n = 5.1$ in the present case; H_n^{max} for 316L SS is 5.5 and the estimated maximum T_{peak}

for each LPBF layer in this work is 2675 K. ε_t in each layer depends on the coefficient of thermal expansion (α_{CTE}) and the difference between T_{peak} and the powder bed temperature (ΔT): $\varepsilon_t = \alpha_{CTE} \Delta T$.

As each of the layers undergo several thermal cycles during LPBF, an accumulated thermal strain is imposed in each layer as building takes place. To estimate ε_t per layer, the temperature drop from T_{peak} should be determined per cycle. Bertoli et al. [49] estimated the temperature
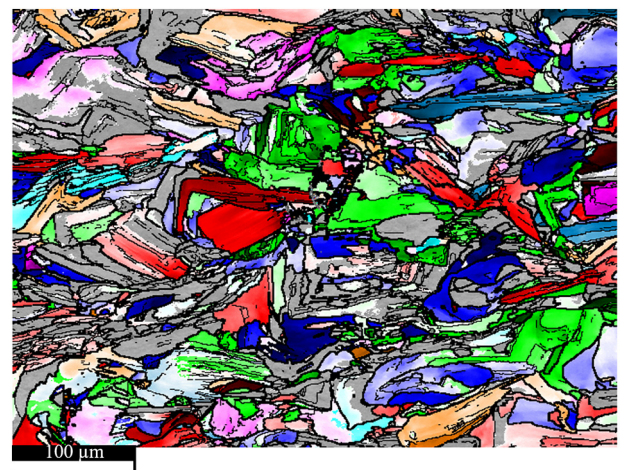

Fig. 5. Texture component map showing the grains with different textures. ⟨110⟩-fibre in green, ⟨111⟩-fibre in blue, ⟨100⟩-fibre in red and Cube component in pink. The rest of the grains have a random texture with a volume fraction lower than 10%.

Table 2
Physical properties of the experimental 316L stainless steel. The thermophysical properties without a corresponding reference have been calculated using Thermo-Calc via TCFE9 database at the liquidus temperature [43].

Material properties	Value at liquidus temperature	Source
A	0.36	[25]
h_s (J/m³)	7.764×10^9	Thermo-Calc
α (m²/s)	6.052×10^{-6}	Thermo-Calc
T_b (K)	2885	Thermo-Calc
T_m (K)	1647	Thermo-Calc
k (W/m·K)	29	[44]
C_p (J/kg·K)	663.614	Thermo-Calc
α_{CTE} (/K)	20.21×10^{-6}	[44]
k (W/m·K)	29	[44]
μ (Pa)	74×10^9	[45]
b (m)	2.54×10^{-10}	[46]
ν	0.3	[46]
c (m/s)	5280	[47]
E_m (J/mol)	73×10^3	[48]
ΔG_{sys} (kJ/mol)	$-(1.69 + 0.013T + 3.1 \times 10^{-5}T^2)$	[9]

gradient (G [K/mm]) for different locations of the 316L SS samples produced by LPBF based on the ratio between P and v:

$$G = 10570\left(\frac{P}{v}\right)^{-0.42}. \tag{10}$$

For a layer thickness of 20 μm, the peak temperature drop per thermal cycle is $\delta = 556$ K. For a hatch distance of 70 μm, the total temperature drop is $\Delta = 1947$ K, which means that at each thermal cycle, the minimum temperature would be $T_{peak} - \Delta = 728$ K (Fig. 6). The average LPBF strain rate can be calculated via [40]:

$$\dot{\varepsilon} = \frac{kT_{peak}v}{P}, \tag{11}$$

where k is the thermal conductivity (Table 2). As the average strain rate of the process is 775 s^{-1}, the interaction time of the laser and powder bed for building a melt pool is $1/\dot{\varepsilon} \sim 1.29$ ms. The estimated thermal cycles that a layer experiences during LPBF of 316L SS and the estimated ε_t in each cycle is depicted in Fig. 6. As illustrated, the as-built material experiences two melting cycles, as well as two solid-state cooling cycles at temperatures higher than $0.5T_m$ (1563 K and 1006 K, respectively), where restoration processes such as DRX and DRV can be activated. As a result of these cycles the material
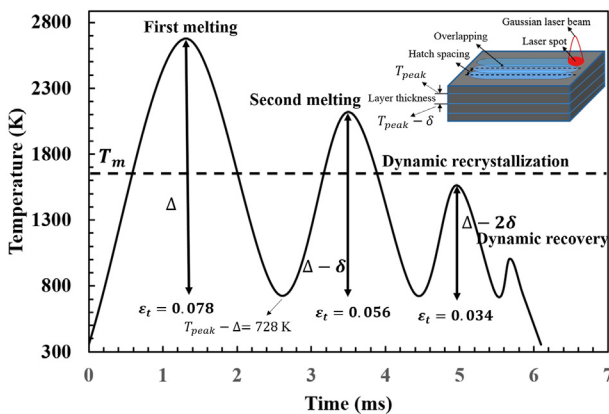
experiences a thermal strain ε_t during each expansion and contraction. The $\varepsilon_t \approx 2 \times (0.039 + 0.028 + 0.017) = 0.168$ per layer.

5.2. Plastic strain

In addition to this, due to the localised and subsequent heating and cooling cycles during LPBF, large thermal gradients are produced in the bulk, which can cause severe plastic deformation of the as-built part during processing. The induced plastic deformation leads to the development of residual strains. When these are large, the high temperature cycles can induce through severe thermo-mechanical processing the activation of restoration mechanisms. Elmesalamy et al. [50] showed that there is a correlation between the residual plastic strains (ε_p) produced during laser welding of 316L SS and the hardness of the bulk material (Fig. 7). We adopted the values of hardness of laser welding in LPBF calculations. The hardness of the as-built sample is 237 ± 4 HV, which yields $\varepsilon_p = 0.14$, as shown in Fig. 7. Therefore, the total strain ($\varepsilon_t + \varepsilon_p$) accumulated in LPBF produced 316L SS in this work is estimated to be 0.308.

6. Discussion

6.1. Evolution of the cellular structure

Fig. 6 shows that the material experiences two rapid solidification cycles, which can lead to the evolution of solidification-enabled cellular structures, in agreement with the previous reports on LPBF-produced 316L SS [15,18,51,52]. The size of these cellular structures can be estimated by both classical and thermostatistical approaches. According to the classical approach, the average cellular structure size d_c can be determined from the cooling rate CR in each cycle [49]:

$$d_c = 80(CR)^{-0.33}. \tag{12}$$

$CR = \dot{\varepsilon}\,\Delta T$, where ΔT is the difference between the T_{peak} at the first and second cycles (2675 K and 2119 K) and the minimum temperature (728 K). The $\dot{\varepsilon} = 775$ s^{-1} (the maximum average strain rate) and $\dot{\varepsilon} = 615$ s^{-1} in first and second cycles, respectively. These are used to estimate the bulk cooling rate at the corresponding cycles. $CR = 1.5 \times 10^6$ K/s and $CR = 8.6 \times 10^5$ K/s for the first and second cycles, respectively, and subsequently, the estimated $d_c = 0.7$ μm and $d_c = 0.88$ μm. Thus, the classical approach yields an average $d_c = 0.79$ μm for the present work (Table 3).

Fig. 6. Estimated thermal cycles in succeeding LPBF layers. The estimated thermal strain in each cycle is shown.
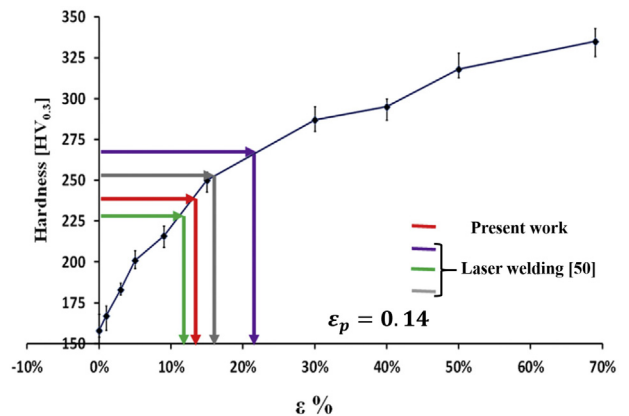

Fig. 7. Correlation between the Vickers hardness ($HV_{0.3}$) with the accumulated plastic strain (ε_p) for laser welded 316L SS [50]. The estimated ε_p for the present work is also indicated on the curve by red arrows.

Table 3
The cellular structure size developed during LPBF, calculated from the classical approach and the thermostatistical approach in first and second thermal cycles, as well as the average values.

Approach	d_c (μm) at the 1st cycle	d_c (μm) at the 2nd cycle	Average d_c (μm)
Classical	0.7	0.88	0.79
Thermostatistical theory[8]	0.5	0.91	0.7

The thermostatistical approach developed in [8] is also able to estimate the cellular structure size. Based on this approach d_c can be estimated via [8]:

$$d_c = \frac{k_c}{\sqrt{\rho_Y}}. \tag{13}$$

Using the values in Table 2, $d_c = 0.5\,\mu m$ and $d_c = 0.91\,\mu m$, in cycles one and two, respectively (Table 3). Therefore, the average cellular structure size estimated by thermostatistical approach is 0.7 μm. The values obtained by both approaches are similar and in agreement with the previous reports on LPBF of 316L SS [15].

6.2. Restoration mechanisms

EBSD observations indicate that the 316L SS produced by LPBF has undergone DRX due to the following reasons. Firstly, as the room temperature stacking fault energy (SFE) of 316L SS is around 64 mJ/m² [53], this alloy is categorised as of medium SFE, and it is thus believed that DDRX is the main restoration mechanism during thermomechanical processing, when a critical strain is reached [54]. As shown in Fig. 6, the alloy experiences two thermal cycles (third and fourth cycles) that are in the temperature ranges of activation of restoration mechanisms (DRV and DRX) at each layer. Considering T_{peak} at third and fourth cycles (1563 K and 1006 K), the corresponding average strain rates are 452 s^{-1} and 292 s^{-1}, respectively. Thus, Z is 10^{18} s^{-1} and 2.2×10^{26} s^{-1} for the third and fourth cycles, respectively. Following eq. (2), $\varepsilon_c = 0.29$ for the third thermal cycle; since $\varepsilon_t + \varepsilon_p > \varepsilon_c$, dynamic recrystallization will occur in agreement with Fig. 2. However, for the fourth cycle $\varepsilon_c = 1.46$, which is far larger than the imposed strain during LPBF. Therefore, DRV is believed to be active at such stage, leading to the formation of substructured grains, as is shown in Fig. 2. Thus, DDRX mechanism is activated in the third thermal cycle of each layer during processing. As a result of DDRX, new strain-free grains form and grow as deformation continues. However, their growth is limited to a certain amount due to an increase in dislocation density with continued deformation, which reduces the driving force for further growth [14].

Adopting eq. (3), the estimated average DDRX grain size of the LPBF produced 316L SS in this study is 4.5 μm. This agrees with the experimentally observed average grain size in the material (4.8 ± 2 μm). However, as shown in Fig. 2b, the grain size distribution is bimodal, suggesting the contribution of continuous dynamic recrystallization to microstructural evolution.

In order to investigate the possibility of CDRX occurrence, and as an alternative approach to the Zener-Hollomon parameter that only considers the process parameters, the thermostatistical approach has been adopted. Using Eq. (4) at 1563 K (peak temperature of the third cycle) and 1006 K (peak temperature of the fourth cycle), $\varepsilon_c = 0.31$ for the third cycle and $\varepsilon_c = 1.48$ for the fourth cycle, which are quite similar to the critical strains estimated by the classical Zener-Hollomon approach. A comparison between the critical strain estimated from classical Zener-Hollomon parameter and thermostatistical approach is given in Table 4. Eq. (4) shows that DDRX is active in the third thermal cycle.

Eq. (6) provides the critical strain rate under which CDRX or DRV can be activated. Using the values in Table 2, $\dot{\varepsilon}_c$ based on the third and fourth peak temperatures is plotted in Fig. 8. It is seen that the third cycle lays on the boundary between CDRX and DRV, although DRV is the predominant mechanism at the fourth cycle, in agreement with the classical approach. Therefore, thermostatistical approach confirms the DRX mechanisms. CDRX is a mechanism for the formation of the new grains via a gradual increase in misorientation between subgrains [55]. As cellular structures form in the first and second cycles of the LPBF, deformation continues into the third cycle, and the dislocation cells formed due to ultra-fast solidification rotate, and their misorientation gradually increases; this occurs during CDRX. Microstructural characterisation is consistent with CDRX taking place during the third cycle, as LAGBs with misorientations in the range of 10–15° are present in the as-built material (Fig. 3b). Fig. 3b shows that ~7% of the LAGBs are in such range, supporting the activation of CDRX [55]. However, CDRX is often accompanied by the evolution of annealing twin boundaries [55], which can hardly be seen in the microstructure, indicating that activation of CDRX is more limited compared with DDRX, which is in agreement with the maps shown in Fig. 8. The occurrence of DRV at the fourth cycle leads to the development of the substructured grains (shown in yellow in Fig. 3). Some of the recrystallized grains also grow during the fourth cycle, appearing as deformed as shown in red in Fig. 3.

The importance of CDRX activation lays on the formation of very fine grains, which display higher dislocation densities compared with DDRX grains that are reportedly dislocation free [55]. This is because the increase in dislocation density of cellular structure is responsible for the increased misorientation of subgrain boundaries during CDRX, as is well established in literature [11]. The present results suggest that subgrain/cellular structures with an estimated size of 0.7 μm were formed by ultra-fast solidification at the first and second thermal cycles for each layer, which also contribute to the high yield and ultimate tensile strength of 316L SS. However, it is still unclear as to the exact role of the cellular structure in the strengthening of LPBF as-built 316L SS [15,56].

Table 4
Critical strain for activation of DDRX during LPBF, calculated from the classical approach and the thermostatistical approach in third and fourth thermal cycles.

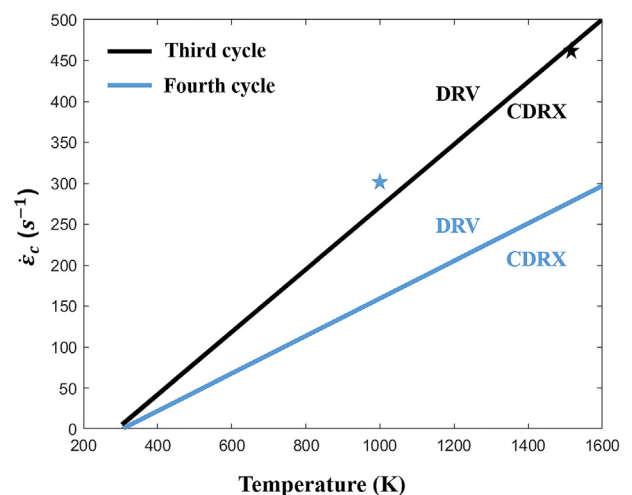| Approach	ε_c at the 3rd cycle	ε_c at the 4th cycle
Classical	0.29	1.46
Thermostatistical theory [8]	0.31	1.48

Fig. 8. Transition map for the activation of CDRX and DRV for the third and fourth thermal cycles in each layer during LPBF of 316L SS.
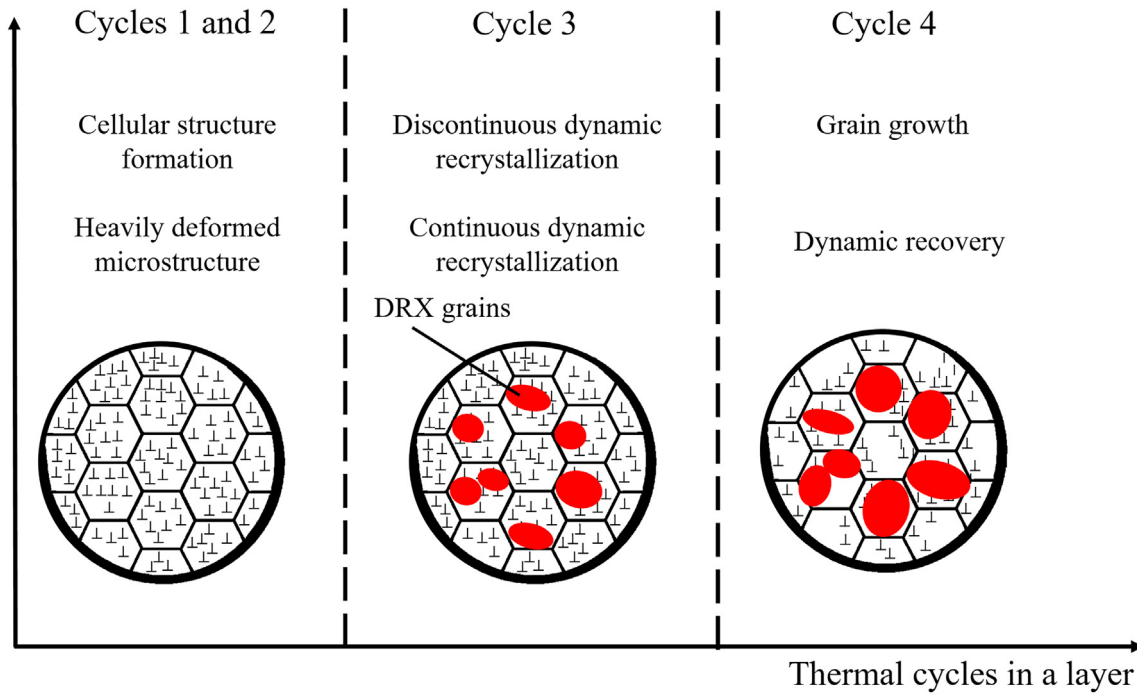
Fig. 9. Summary of the microstructural evolution during different LPBF thermal cycles.

6.3. Microstructure evolution during LPBF

The microstructure of the as-built LPBF 316L SS is influenced by the complex repetitive thermo-mechanical processing illustrated in Fig. 6. The presented methodology aims to simulate the whole process with a good level of certainty, as the exact simulation of the LPBF process physics is quite challenging. The gradual reduction in strain, strain rate and temperature, which are the key factors for describing the thermo-mechanical processes during LPBF, are approximated for each layer during LPBF. It should also be considered that due to the inhomogeneous thermal and plastic deformation imposed

during processing, a grain may undergo several recovery mechanisms. The overall process of microstructure evolution of 316L SS during various thermal cycles of LPBF is schematically depicted in Fig. 9. The fundamental understanding of the microstructure evolution during LPBF that is presented in this work aims to reduce the unclear issues related to microstructure-processing-relationships in LPBF.

Future work will consider incomplete builds, where the effects of layering can be individually recognised, this can be combined with X-ray diffraction (XRD) to quantify dislocation density per layer; however, such study is beyond the scope of this work.
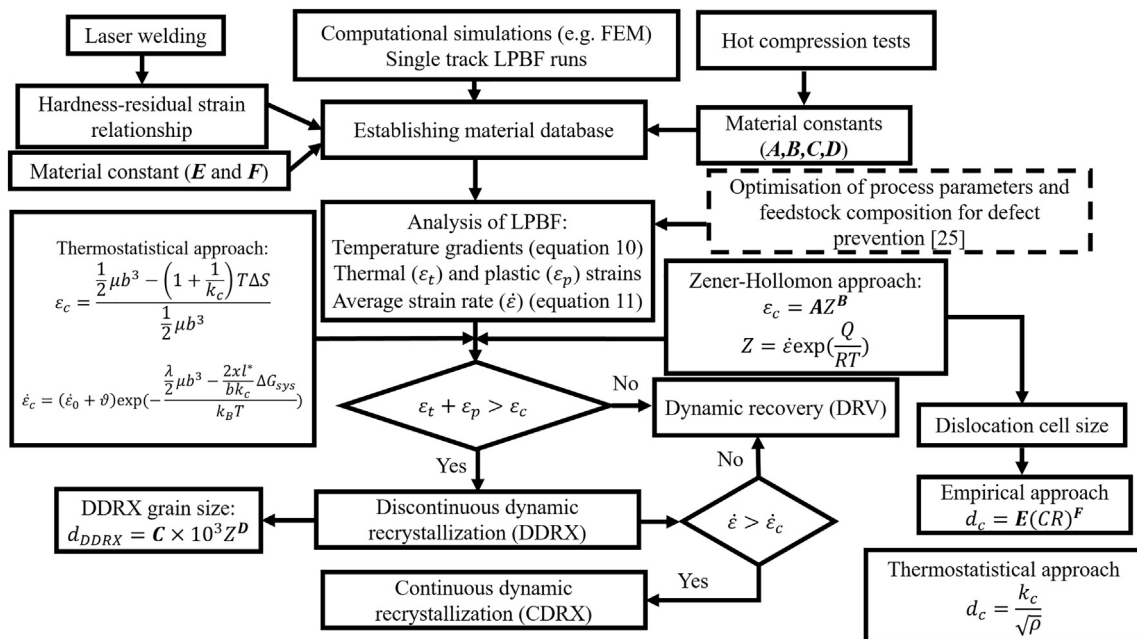

Fig. 10. Schematic microstructural development during LPBF.

6.4. Tailoring microstructure in LPBF: Alloy design

Microstructure control determines the mechanical behaviour in commercial alloys. In conventional manufacturing methods, such as casting and forming, certain procedures are well-established for process control. While, in LPBF, there is no clear methodology to tailor microstructures as of yet in order to control the mechanical properties. Here we summarise the methodology presented in this work; this can be adopted for alloy and microstructure design for metal additive manufacturing. LPBF is a manufacturing approach with *in situ* thermo-mechanical processing. Therefore, hot restoration processes should be described and optimised to get the best possible mechanical properties.

The flowchart presented in Fig. 10 shows a method to tailor microstructural evolution to optimise the build mechanical properties. The first step is to establish a material database; this will include constants *A*, *B*, *C*, *D*, *E* and *F* used to compute the critical strain via the Zener-Hollomon approach, the DDRX grain size, and the cell size via the empirical approach, as shown in Fig. 10. Hot compression tests at various temperatures, strain rates and strains give information on the material's constants, leading to an estimation of the energy required to activate DRX, the critical strain for DRX and the average DRX grain and dislocation cell size. Processes such as laser welding can be used to estimate the residual strain accumulated during LPBF processing. Laser welding can also be used to simulate the dislocation cell size when the cooling rates are comparable to LPBF [57]. Before analysing microstructure-related phenomena, it is necessary to optimise both the LPBF process parameters and the feedstock composition to avoid the formation of solidification cracks, pores such as keyholes and lack of fusion and defects such as balling. Previous work by the authors on LPBF crack and porosity control [25], in combination with processing optimisation to produce defect-free samples must be taken into account [58–61]. The next input is the estimation of temperature gradients, ε_t and ε_p and the average strain rate of the LPBF process, both in the whole bulk and in a single layer. Computational models, such as the finite element method (FEM), empirical equations and single track LPBF runs, can be useful to estimate such inputs to the material database. In this work, we have used eqs. (10) and (11) for temperature gradients across the build and $\dot{\varepsilon}$. Details for the estimation of ε_t and ε_p are also presented, although any other computational methods or relationships can be used to feed into the material database. The strategy presented here can be applied to control grain size and recrystallization in as-built LPBF components. Both classical approaches such as the Zener-Hollomon approach, and the more recent thermostatistical approach can be employed to control the LPBF process parameters based on the possibility of activation of DRX and DRV.

The methodology presented in this work (Fig. 10) can be applied to other alloying systems, such as 17–4 precipitation-hardening stainless steels and Ti-6Al-4V, in which the occurrence of DRX can significantly affect the yield strength of as-built alloys. There are several reports on the suppression of martensite formation and stabilisation of austenite in LPBF produced 17–4 precipitation-hardening stainless steels, which may be related to the formation of fully recrystallized austenite grains [62,63]. It is also well-known that the yield strength of LPBF Ti-6Al-4V is also dependent on process parameters and subsequently the thermo-mechanical processing that the alloy experiences during LPBF [64–66]. Thus, the methodology presented here will minimise the discrepancies in properties and microstructures when various alloy families are subjected to LPBF.

7. Conclusions

Thermo-mechanical processing during laser powder bed fusion is studied in an austenitic 316L stainless steel. A very fine grain structure is obtained in the as-built part, leading to an outstanding combination of the yield and ultimate tensile strength. Microstructural investigations revealed the signatures of different recrystallization mechanisms, as well as of dynamic recovery. The physical metallurgical aspects of laser powder bed fusion depend on thermal and plastic strains, as well as temperature and strain rate variations are considered. Based on such estimations, restoration mechanisms during laser powder bed fusion are modelled via classical and thermostatistical approaches to predict microstructure development.

For the process parameters considered in this investigation, each layer experiences four thermal cycles during building. The first two cycles incorporate rapid melting and solidification, leading to a heavily deformed cellular structure. A high density of fresh dislocation-free recrystallized grains is developed via dynamic recrystallization in the third cycle. Dynamic recovery is the principal mechanism governing in the fourth thermal cycle.

Due to the non-uniform nature of deformation generated during laser powder bed fusion, the dislocation density across the grain structure is unequal, causing a composite-like effect leading to the best combination of yield and ultimate tensile strength that has so far been reported in the literature. This microstructure evolution confirms that the final microstructures of laser powder bed fusion materials are strongly dependent on the process parameters; the optimisation of such parameters resulted in the outstanding strength values of the as-built material. A methodology for tailoring microstructural evolution by tailoring dynamic recrystallization for different types of alloys is also presented; this can be adopted as a guide for alloy and microstructure design, and for process optimisation.

Data availability

The processed data required to reproduce these findings cannot be shared at this time as the data also forms part of an ongoing study.

Declaration of Competing Interest

The authors declare that they have no known competing financial interests or personal relationships that could have appeared to influence the work reported in this paper.

References

[1] R. Casati, J. Lemke, M. Vedani, Microstructure and fracture behavior of 316L austenitic stainless steel produced by selective laser melting, J. Mater. Sci. Tech. 32 (8) (2016) 738–744.

[2] M.J. Matthews, G. Guss, S.A. Khairallah, A.M. Rubenchik, P.J. Depond, W.E. King, Denudation of metal powder layers in laser powder bed fusion processes, Acta Mater. 114 (2016) 33–42.

[3] E. Mirkoohi, H.-C. Tran, Y.-L Lo, Y.-C. Chang, H.-Y. Lin, S.Y. Liang, Analytical mechanics modeling of residual stress in laser powder bed considering flow hardening and softening, Int. J. Adv. Manuf. Technol. (2020) 1–14.

[4] U. Kocks, H. Mecking, Physics and phenomenology of strain hardening: the fcc case, Prog. Mater. Sci. 48 (3) (2003) 171–273.

[5] M.A. Galindo-Fernández, K. Mumtaz, P.E.J. Rivera-Daz-del-Castillo, E.I. Galindo-Nava, H. Ghadbeigi, A microstructure sensitive model for deformation of Ti-6Al-4V describing cast-and-wrought and additive manufacturing morphologies, Mater. Des. 160 (2018) 350–362.

[6] X.-g. Liu, L.-g. Zhang, R.-s. Qi, L. Chen, M. Jin, B.-f. Guo, Prediction of critical conditions for dynamic recrystallization in 316LN austenitic steel, J. Iron Steel Res. Int. 23 (3) (2016) 238–243.

[7] C. Zener, J.H. Hollomon, Effect of strain rate upon plastic flow of steel, J. Appl. Phys. 15 (1) (1944) 22–32.

[8] E.I. Galindo-Nava, P.E.J. Rivera-Daz-del-Castillo, Grain size evolution during discontinuous dynamic recrystallization, Scr. Mater. 72 (2014) 1–4.

[9] E.I. Galindo-Nava, P.E.J. Rivera-Daz-del-Castillo, Thermostatistical modelling of hot deformation in FCC metals, Int. J. Plast. 47 (2013) 202–221.

[10] R.D. Doherty, D.A. Hughes, F.J. Humphreys, J.J. Jonas, D.J. Jensen, M.E. Kassner, W.E. King, T.R. McNelley, H.J. McQueen, A.D. Rollett, Current issues in recrystallization: a review, Mater. Sci. Eng. A 238 (2) (1997) 219–274.

[11] K. Huang, R. Logé, A review of dynamic recrystallization phenomena in metallic materials, Mater. Des. 111 (2016) 548–574.

[12] H.J. McQueen, S. Yue, N.D. Ryan, E. Fry, Hot working characteristics of steels in austenitic state, J. Mater. Process. Technol. 53 (1–2) (1995) 293–310.

[13] A. Dehghan-Manshadi, M.R. Barnett, P.D. Hodgson, Hot deformation and recrystallization of austenitic stainless steel: Part I. Dynamic recrystallization, Metall. Mater. Trans. A 39 (6) (2008) 1359–1370.

[14] R. Puli, G.J. Ram, Dynamic recrystallization in friction surfaced austenitic stainless steel coatings, Mater. Charact. 74 (2012) 49–54.

[15] Y.M. Wang, T. Voisin, J.T. McKeown, J. Ye, N.P. Calta, Z. Li, Z. Zeng, Y. Zhang, W. Chen, T.T. Roehling, et al., Additively manufactured hierarchical stainless steels with high strength and ductility, Nat. Mater. 17 (1) (2018) 63–71.

[16] J.P. Oliveira, A. LaLonde, J. Ma, Processing parameters in laser powder bed fusion metal additive manufacturing, Mater. Des. 193 (2020) 108762.

[17] Z. Sun, X. Tan, S.B. Tor, C.K. Chua, Simultaneously enhanced strength and ductility for 3D-printed stainless steel 316L by selective laser melting, NPG Asia Mater. 10 (4) (2018) 127.

[18] Z. Sun, X. Tan, S.B. Tor, W.Y. Yeong, Selective laser melting of stainless steel 316L with low porosity and high build rates, Mater. Des. 104 (2016) 197–204.

[19] K.A. Babu, Y.H. Mozumder, R. Saha, V.S. Sarma, S. Mandal, Hot-workability of super-304H exhibiting continuous to discontinuous dynamic recrystallization transition, Mater. Sci. Eng. A 734 (2018) 269–280.

[20] M. Tikhonova, R. Kaibyshev, A. Belyakov, Microstructure and mechanical properties of austenitic stainless steels after dynamic and post-dynamic recrystallization treatment, Adv. Eng. Mater. 20 (7) (2018) 1700960.

[21] H. Zhang, H. Xiao, X. Fang, Q. Zhang, R. Logé, K. Huang, A critical assessment of experimental investigation of dynamic recrystallization of metallic materials, Mater. Des. 108873 (2020).

[22] Y.H. Mozumder, K.A. Babu, R. Saha, V.S. Sarma, S. Mandal, Dynamic microstructural evolution and recrystallization mechanism during hot deformation of intermetallic-hardened duplex lightweight steel, Mater. Sci. Eng. A 139613 (2020).

[23] H. Eskandari Sabzi, P.E.J. Rivera-Daz-del-Castillo, Defect prevention in selective laser melting components: compositional and process effects, Materials 12 (22) (2019) 3791.

[24] T.T. Roehling, S.S.Q. Wu, S.A. Khairallah, J.D. Roehling, S.S. Soezeri, M.F. Crumb, M.J. Matthews, Modulating laser intensity profile ellipticity for microstructural control during metal additive manufacturing, Acta Mater. 128 (2017) 197–206.

[25] H. Eskandari Sabzi, S. Maeng, X. Liang, M. Simonelli, N.T. Aboulkhair, P.E.J. Rivera-Daz-del-Castillo, Controlling crack formation and porosity in laser powder bed fusion: alloy design and process optimisation, Addit. Manuf. 101360 (2020).

[26] A. Riemer, S. Leuders, M. Thöne, H. Richard, T. Tröster, T. Niendorf, On the fatigue crack growth behavior in 316L stainless steel manufactured by selective laser melting, Eng. Fract. Mech. 120 (2014) 15–25.

[27] J. Suryawanshi, K. Prashanth, U. Ramamurty, Mechanical behavior of selective laser melted 316L stainless steel, Mater. Sci. Eng. A 696 (2017) 113–121.

[28] M. Pham, B. Dovgyy, P. Hooper, Twinning induced plasticity in austenitic stainless steel 316L made by additive manufacturing, Mater. Sci. Eng. A 704 (2017) 102–111.

[29] T. Larimian, M. Kannan, D. Grzesiak, B. AlMangour, T. Borkar, Effect of energy density and scanning strategy on densification, microstructure and mechanical properties of 316L stainless steel processed via selective laser melting, Mater. Sci. Eng. A 770 (2020) 138455.

[30] E. Liverani, S. Toschi, L. Ceschini, A. Fortunato, Effect of selective laser melting (SLM) process parameters on microstructure and mechanical properties of 316L austenitic stainless steel, J. Mater. Process. Tech. 249 (2017) 255–263.

[31] F. Bartolomeu, M. Buciumeanu, E. Pinto, N. Alves, O. Carvalho, F.S. Silva, G. Miranda, 316L stainless steel mechanical and tribological behavior—a comparison between selective laser melting, hot pressing and conventional casting, Addit. Manuf. 16 (2017) 81–89.

[32] R. Shrestha, J. Simsiriwong, N. Shamsaei, Fatigue behavior of additive manufactured 316L stainless steel parts: effects of layer orientation and surface roughness, Addit. Manuf. 28 (2019) 23–38.

[33] J. Boes, A. Röttger, L. Becker, W. Theisen, Processing of gas-nitrided AISI 316L steel powder by laser powder bed fusion–microstructure and properties, Addit. Manuf. 30 (2019) 100836.

[34] M.J. Heiden, L.A. Deibler, J.M. Rodelas, J.R. Koepke, D.J. Tung, D.J. Saiz, B.H. Jared, Evolution of 316L stainless steel feedstock due to laser powder bed fusion process, Addit. Manuf. 25 (2019) 84–103.

[35] A. Leicht, M. Rashidi, U. Klement, E. Hryha, Effect of process parameters on the microstructure, tensile strength and productivity of 316L parts produced by laser powder bed fusion, Mater. Charact. 159 (2020) 110016.

[36] L. Liu, Q. Ding, Y. Zhong, J. Zou, J. Wu, Y.-L. Chiu, J. Li, Z. Zhang, Q. Yu, Z. Shen, Dislocation network in additive manufactured steel breaks strength–ductility trade-off, Mater. Today 21 (4) (2018) 354–361.

[37] Y. Liu, Y. Yang, S. Mai, D. Wang, C. Song, Investigation into spatter behavior during selective laser melting of AISI 316L stainless steel powder, Mater. Des. 87 (2015) 797–806.

[38] Q. Lu, N. Nguyen, A. Hum, T. Tran, C. Wong, Optical in-situ monitoring and correlation of density and mechanical properties of stainless steel parts produced by selective laser melting process based on varied energy density, J. Mater. Process. Tech. 271 (2019) 520–531.

[39] A.J. Dunbar, E.R. Denlinger, J. Heigel, P. Michaleris, P. Guerrier, R. Martukanitz, T.W. Simpson, Development of experimental method for in situ distortion and temperature measurements during the laser powder bed fusion additive manufacturing process, Addit. Manuf. 12 (2016) 25–30.

[40] H. Eskandari Sabzi, P.E.J. Rivera-Daz-del-Castillo, Composition and process parameter dependence of yield strength in laser powder bed fusion alloys, Mater. Des. 109024 (2020).

[41] D. Hann, J. Iammi, J. Folkes, A simple methodology for predicting laser-weld properties from material and laser parameters, J. Phy. D. App. Phys. 44 (44) (2011) 445401.

[42] R. Fabbro, Scaling laws for the laser welding process in keyhole mode, J. Mater. Process. Technol. 264 (2019) 346–351.

[43] J.-O. Andersson, T. Helander, L. Höglund, P. Shi, B. Sundman, Thermo-Calc & DICTRA, computational tools for materials science, Calphad 26 (2) (2002) 273–312.

[44] W. Jiang, Y. Zhang, W. Woo, Using heat sink technology to decrease residual stress in 316L stainless steel welding joint: finite element simulation, Int. J. Pressure. Vessels. Piping. 92 (2012) 56–62.

[45] E. Puchi Cabrera, High temperature deformation of 316L stainless steel, Mater. Sci. Technol. 17 (2) (2001) 155–161.

[46] C. Robertson, M. Fivel, A. Fissolo, Dislocation substructure in 316L stainless steel under thermal fatigue up to 650 K, Mater. Sci. Eng. A 315 (1–2) (2001) 47–57.

[47] L.M. Headings, K. Kotian, M.J. Dapino, Speed of sound measurement in solids using polyvinylidene fluoride (PVDF) sensors, ASME 2013 Conference on Smart Materials, Adaptive Structures and Intelligent Systems, American Society of Mechanical Engineers Digital Collection, 2013.

[48] R.E. Smallman, R.J. Bishop, Modern Physical Metallurgy and Materials Engineering, Elsevier, 1999.

[49] U.S. Bertoli, B.E. MacDonald, J.M. Schoenung, Stability of cellular microstructure in laser powder bed fusion of 316L stainless steel, Mater. Sci. Eng. A 739 (2019) 109–117.

[50] A. Elmesalamy, J. Francis, L. Li, A comparison of residual stresses in multi pass narrow gap laser welds and gas-tungsten arc welds in AISI 316L stainless steel, Int. J. Pressure. Vessels. Piping. 113 (2014) 49–59.

[51] H. Choo, K.-L. Sham, J. Bohling, A. Ngo, X. Xiao, Y. Ren, P.J. Depond, M.J. Matthews, E. Garlea, Effect of laser power on defect, texture, and microstructure of a laser powder bed fusion processed 316L stainless steel, Mater. Design. 164 (2019) 107534.

[52] M. Zhang, C.-N. Sun, X. Zhang, J. Wei, D. Hardacre, H. Li, Predictive models for fatigue property of laser powder bed fusion stainless steel 316L, Mater. Des. 145 (2018) 42–54.

[53] S.G. Chowdhury, P. Sahu, B. Mahato, P.K. De, Evolution of recrystallization texture in AISI300 series austenitic stainless steels after cold rolling to large strain, Microstructure and Texture in Steels, Springer 2009, pp. 361–378.

[54] M. Hajian, A. Abdollah-Zadeh, S. Rezaei-Nejad, H. Assadi, K. Chung, M. Shokouhimehr, Microstructure and mechanical properties of friction stir processed AISI 316L stainless steel, Mater. Des. 67 (2015) 82–94.

[55] F.J. Humphreys, M. Hatherly, Recrystallization and Related Annealing Phenomena, Elsevier, 2012.

[56] Z. Li, B. He, Q. Guo, Strengthening and hardening mechanisms of additively manufactured stainless steels: the role of cell sizes, Scr. Mater. 177 (2020) 17–21.

[57] S. Katayama, A. Matsunawa, Solidification microstructure of laser welded stainless steels, International Congress on Applications of Lasers & Electro-Optics, vol. 1984, Laser Institute of America 1984, pp. 60–67.

[58] A.G. Demir, B. Previtali, Investigation of remelting and preheating in SLM of 18Ni300 maraging steel as corrective and preventive measures for porosity reduction, Int. J. Adv. Manuf. Technol. 93 (5–8) (2017) 2697–2709.

[59] W. Stopyra, K. Gruber, I. Smolina, T. Kurzynowski, B. Kuźnicka, Laser powder bed fusion of AA7075 alloy: influence of process parameters on porosity and hot cracking, Addit. Manuf. 101270 (2020).

[60] R. Seede, D. Shoukr, B. Zhang, A. Whitt, S. Gibbons, P. Flater, A. Elwany, R. Arroyave, I. Karaman, An ultra-high strength martensitic steel fabricated using selective laser melting additive manufacturing: densification, microstructure, and mechanical properties, Acta Mater. 186 (2020) 199–214.

[61] L. Johnson, M. Mahmoudi, B. Zhang, R. Seede, X. Huang, J.T. Maier, H.J. Maier, I. Karaman, A. Elwany, R. Arróyave, Assessing printability maps in additive manufacturing of metal alloys, Acta Mater. 176 (2019) 199–210.

[62] F.S. Freeman, J. Sharp, J. Xi, I. Todd, Influence of solidification cell structure on the martensitic transformation in additively manufactured steels, Addit. Manuf. 30 (2019) 100917.

[63] S. Vunnam, A. Saboo, C. Sudbrack, T.L. Starr, Effect of powder chemical composition on the as-built microstructure of 17-4 PH stainless steel processed by selective laser melting, Addit. Manuf. 30 (2019) 100876.

[64] H. Ali, H. Ghadbeigi, K. Mumtaz, Processing parameter effects on residual stress and mechanical properties of selective laser melted Ti6Al4V, J. Mater. Eng. Perform. 27 (8) (2018) 4059–4068.

[65] C. Pauzon, P. Forêt, E. Hryha, T. Arunprasad, L. Nyborg, Argon-helium mixtures as laser-powder bed fusion atmospheres: towards increased build rate of Ti-6Al-4V, J. Mater. Process. Technol. 279 (2020) 116555.

[66] Z. Zou, M. Simonelli, J. Katrib, G. Dimitrakis, R. Hague, Refinement of the grain structure of additive manufactured titanium alloys via epitaxial recrystallization enabled by rapid heat treatment, Scr. Mater. 180 (2020) 66–70.